

Enhanced Supercapacitance Performance of Hierarchically Porous Carbon Obtained from *Terminalia bellirica* (Barro) Seed Stone

Sarita Manandhar,^{†,¶} Chhabi Lal Gnawali,[#] Rinita Rajbhandari,[#] Renzhi Ma,[†] Jonathan P. Hill,[†] Katsuhiko Ariga,^{†,‡} Lok Kumar Shrestha^{†,¶,*}

[†]Research Center for Materials Nanoarchitectonics (MANA), National Institute for Materials Science (NIMS), 1-1 Namiki, Tsukuba, Ibaraki 305-0044, Japan

[¶]Department of Materials Science, Institute of Pure and Applied Sciences, University of Tsukuba, 1-1-1 Tennodai, Tsukuba, Ibaraki 305-8573, Japan

[#]Department of Applied Sciences and Chemical Engineering, Pulchowk Campus, Institute of Engineering (IOE), Tribhuvan University, 44700 Lalitpur, Nepal

[‡]Department of Advanced Materials Science, Graduate School of Frontier Sciences, The University of Tokyo, 5-1-5 Kashiwanoha, Kashiwa, Chiba 277-8561, Japan

KEYWORDS: *Terminalia bellirica* seed, ZnCl₂ activation, hierarchical porous carbon, EDLC, supercapacitor.

ABSTRACT: Biomass carbons are promising candidates for energy storage applications due to their large surface areas, hierarchical pore structures, well-defined pore dimensions and tunable porosity. Here, we report the production of porous carbon materials from *Terminalia bellirica* (Barro) seeds involving zinc chloride activation at different impregnation ratios (1:1 – 1:3) and carbonization temperatures (700 – 900 °C), and their supercapacitive performances in 1 M sulfuric acid in three-electrode and two-electrode systems. The material carbonized at 700 °C at the impregnation ratio of 1:3 exhibited a high specific surface area of 2301 m²·g⁻¹ and large pore volume of 1.887 cm³·g⁻¹. Electrochemical analyses revealed an electrical double-layer charge storage mechanism, and the electrode achieved a maximum specific capacitance of 365.4 F·g⁻¹ at 1 A·g⁻¹ with excellent capacitance retention of 66.0% even at 50 A·g⁻¹. The symmetric supercapacitor cell assembled using this material delivered an energy density of 7.1 W·hkg⁻¹ at a power density of 600 W·kg⁻¹ retaining 98.2% cycle life after 10,000 charge/discharge cycles. These results indicate that there is a great potential in using Barro seed as a sustainable carbon source for the fabrication of high surface area activated carbons for energy storage supercapacitor applications.

1. INTRODUCTION

Global industrialization has led to a significant increase in energy demands. The Global Bioenergy Statistics (GBS) Reports of 2022 and 2024 revealed that 80% of the primary energy supply is obtained from fossil fuels, 15% from renewable sources, and 5% from nuclear power. In 2022, global energy consumption amounted to 422 exajoules (EJ) and was dominated by fossil fuels with an over 82% share. In 2023, global renewable electricity generation reached 8,931 terawatt hour (TWh) of which bioenergy contributed 697 TWh (8%) being the fourth largest renewable source, increasing from 685 TWh in 2020.¹ The depletion of fossil fuels causes health and environmental

issues that have led to an urgent requirement for the development of green, sustainable and renewable energy storage systems.²⁻⁴ With the burgeoning demand for renewable energy sources, biomass is being widely acknowledged due to its potential to contribute to climate and energy goals. For the proper harvesting and intermittent supply of energy from these renewable sources, advanced energy storage technologies, including rechargeable batteries and supercapacitors (SCs) have been investigated and proposed.⁵

SCs have significant advantages, such as rapid charge/discharge, high power density, long cyclic stability, wide operational temperature ranges and safety of operation compared to lithium-ion batteries.⁵⁻¹⁰ Recently, SCs have found wide applications in electronics, transportation, medical equipment, and their use is also growing in other technical fields.⁵ Nevertheless, SCs suffer from the disadvantage of their low energy density.¹¹ To enhance the energy performance of SCs, various electrode materials such as activated carbons, fullerenes, carbon nanotubes, graphene, and carbon nanohorns have been explored.¹²⁻¹⁷ Other cost-efficient materials that can be used are earth abundant transition metal oxides/hydroxides such as MnO₂, Fe₃O₄, Ni(OH)₂, etc., industrial waste like coal tar pitch, sewage sludge, etc., conductive polymers as polypyrrole, polyaniline, etc., iron-based compounds, reduced graphene oxide, etc.¹⁸⁻¹⁹ Of these, nanoporous carbons prepared from biomass have emerged as the most promising candidates for use as high-performance electrode materials due to their ultrahigh specific surface area, well-developed porosity, high conductivity and chemical stability. Furthermore, the utilization of renewable carbon sources prioritizes agricultural waste, aligning with the principles of green chemistry and sustainability.²⁰⁻²²

Various nanoporous activated carbons have been prepared using different biomass sources such as *Terminalia chebula* seed,²³ *Phoenix dactylifera* seed,²⁴ rice husk,²⁵ mung bean husk,²⁶ pomelo peel,²⁷ walnut shell,²⁸ lychee seed,²⁹ *Platanus achene* fibers,³⁰ and so on. Various strategies

exist for their preparation including carbonization (pyrolysis, hydrothermal, laser-induced, microwave-assisted), pretreatment, template assisted, chemical vapor deposition and activation (physical and chemical).³¹ Chemical activation is preferred over other methods to enhance the surface textural properties. Inorganic salts, acids, and bases have been explored as the chemical activators with commonly used activators being potassium chloride (KCl), zinc chloride (ZnCl₂), phosphoric acid (H₃PO₄), sulfuric acid (H₂SO₄), potassium hydroxide (KOH), and sodium hydroxide (NaOH).^{2,21} The implementation of various synthesis strategies, activating agents along with change in carbonization time plays an important role in tailoring the pore structures that profoundly affects the electrochemical performance of the electrode materials. The presence of macropores acts as ion reservoir that facilitates fast electrolyte diffusion, mesopores help in ion transport whereas micropores provide large surface area for charge storage enhancing the capacitive performance of the materials.^{32,33} Previous studies have demonstrated that ZnCl₂ activation leads to the formation of microporous carbon due to dehydration and depolymerization of biochar. It effectively eliminates hydrogen and oxygen as water from the biomass precursor.^{5,34-36} By optimizing the synthetic conditions, particularly impregnation ratio and carbonization temperature, a subtle balance of micro- and mesopores can be achieved. Such hierarchical micro- and mesoporous carbon enhances the supercapacitance performance of the resulting materials by promoting electrolyte ion diffusion.³⁴

This work reports the synthesis and supercapacitive performance of the ultra-high surface area hierarchically porous carbon materials derived from *Terminalia bellirica* (Barro) seed involving ZnCl₂ activation. The effects of the precursor/ZnCl₂ mixing ratio (1:1, 1:2 and 1:3) and carbonization temperature (700 - 900 °C) on surface area and porosity properties of the products were systematically studied. Electrochemical characterization was carried out using an aqueous

electrolyte (1 M H₂SO₄). The electrode prepared from the material having optimal surface area (2301 m²·g⁻¹) exhibited a high specific capacitance of 365.4 F·g⁻¹ at 1 A·g⁻¹ current density in a three-electrode system. In addition, a symmetrical supercapacitor cell assembled using this material delivered a good energy density of 7.1 W·hkg⁻¹ at a power density of 600 W·kg⁻¹ accompanied by excellent cycle life of 98.2% after 10,000 cycles. These results demonstrate that Barro seed serves as a sustainable carbon source for the production of the high surface area porous carbon materials essential for high performance supercapacitor applications.

2. EXPERIMENTAL SECTION

2.1. Fabrication of nanoporous activated carbon materials. *Terminalia bellirica* (Barro) seed was washed several times with distilled water and dried before grinding to a powder form. The precursor powder was mixed with ZnCl₂ in 1:1 weight ratio and carbonized at different temperatures from 700 – 900 °C in a tube furnace under a continuous flow of nitrogen gas (120 cc min⁻¹) for 4 h. Similarly, the precursor was chemically activated with ZnCl₂ at different mixing ratios (1:1, 1:2 and 1:3) and carbonized at 700 °C. The carbonized samples were treated with 0.1 M hydrochloric acid (HCl) solution followed by distilled water washing for several times until the supernatant liquid attained pH ~ 7. The products obtained were dried at 80 °C for 6 h under reduced pressure and are referred to as BrC_Zx_y; where x (1,2, and 3) represents ratio of mixing with ZnCl₂, and y = carbonization temperature (700, 800, and 900 °C). Thus, the ZnCl₂ activated samples have been named as BrC_Z1_700, BrC_Z2_700, and BrC_Z3_700 with varying impregnation ratio and BrC_Z1_800 and BrC_Z1_900 with varying carbonization temperature. A reference carbon sample was prepared by direct carbonization of the precursor powder at 700 °C in the absence of ZnCl₂ and is designated as BrP_700.

2.2. Characterizations. Barro precursor and the derived carbon samples were characterized

using different techniques, including thermogravimetric analysis (TGA) with the sample under nitrogen environment using a SII instrument (Model Exstar 600), powder X-ray diffraction (XRD: Rigaku X-ray diffractometer RINT, Japan, Cu-K α radiation, operated at 40 kV and 40 mA at 25 °C), Raman scattering spectroscopy (NRS-3100, JASCO, Tokyo, Japan), Fourier-transform infrared (FTIR) spectroscopy (NICOLET iS20, Thermo-Fisher Scientific, Waltham, MA, USA), scanning electron microscopy (SEM: S-4800, Hitachi Co. Ltd., Tokyo, Japan, operated at 10 kV and 10 μ A), transmission electron microscopy (TEM: JEOL Model JEM3100F, Tokyo, Japan, operated at 300 kV), and nitrogen adsorption-desorption isothermometry (Quantachrome Autosorb-iQ2, Boynton Beach, FL, USA). Density functional theory (DFT) and Barrett-Joyner-Halenda (BJH) methods were used to calculate the pore dimensions and pore volumes. Surface composition of prepared carbon samples was studied using X-ray photoelectron spectroscopy (XPS) (Quantera SXM instrument, ULVACPHI, Chanhassen, MN, USA).

2.3. Electrochemical measurements. Supercapacitance properties were studied in both three-electrode and two-electrode systems in 1 M H₂SO₄ aqueous electrolyte solution. Cyclic voltammetry (CV), galvanostatic charge/discharge (GCD) and electrochemical impedance spectroscopy (EIS) measurements were performed at 25 °C. The working electrode was prepared on graphite sheet (1 \times 3 cm²). The graphite sheet was sonicated with 3 M HCl for 30 min, washed several times with distilled water then with ethanol, and dried at 80 °C for 3 h. The carbon sample was ground into a fine powder and mixed (also by grinding) with poly(vinylidene fluoride) (PVDF) and carbon black (acetylene) at 80:10:10 weight % ratio. The above mixture was mixed with N-methyl-2-pyrrolidone (NMP) forming a slurry, which was spread on a cleaned graphite sheet (1 \times 1 cm²) followed by drying at 80 °C overnight. The weight of active carbon material was in the range of 1.5-1.9 mg. CV, GCD and EIS measurements were performed using a Biologic

potentiostat (Bio-Logic SAS, model VSP-3e, France) using Ag/AgCl and platinum (Pt) wire as reference and counter electrodes, respectively. The specific capacitance (C_s) of the electrodes were calculated using Eq 1:

$$C_s = \frac{I \times t_d}{m \times \Delta V} \dots\dots\dots (1)$$

where, I (A), t_d (s), m (g) and ΔV (V) are discharge current, discharge time, mass of active electrode material and operating voltage, respectively.

Based on CV curves, the surface- and diffusion-controlled contributions were studied in order to understand the charge-discharge dynamics. The relationship between scan rate (v) and current density (i) is shown (Eq 2):

$$i = av^b \dots\dots\dots (2)$$

where, i ($A \cdot g^{-1}$) is the sum current contribution of surface-controlled (capacitive) and diffusion-controlled current, a and b are constants, and v is scan rate ($mV \cdot s^{-1}$). If $b \approx 1$, the surface-controlled process dominates the charge storage mechanism, which is typical for electric double-layer capacitance or pseudo-capacitance. If $b \approx 0.5$, then the diffusion-controlled energy storage mechanism occurs, where the current is governed by the diffusion of ions within the bulk of the electrode material.³⁷ The surface-controlled and diffusion controlled current contribution can be calculated quantitatively using the following equation (Eq 3):³⁸⁻⁴⁰

$$i(V) = k_1 v + k_2 v^{1/2} \dots\dots\dots (3)$$

where, i , v , k_1 , and k_2 are total current, scan rate, and constants, respectively.

For symmetric supercapacitor cells, the energy density and power density were calculated according to the following equations:

1
2
3
4
5
6
7
8
9
$$E = \frac{0.5 \times C_s \times (\Delta V)^2}{3.6} \dots\dots\dots (4)$$

10
11
12
13
14
15
16
17
18
19
20
21
$$P = \frac{3600 \times E}{t_d} \dots\dots\dots (5)$$

22
23
24
25
26
27
28
29
30
31
32
33
34
35
36
37
38
39
40
41
42
43
44
45
46
47
48
49
50
51
52
53
54
55
56
57
58
59
60
where, E ($\text{W} \cdot \text{hkg}^{-1}$) is energy density and P ($\text{W} \cdot \text{kg}^{-1}$) is power density.³⁷

3. RESULTS AND DISCUSSION

The FTIR spectrum of the precursor (Figure 1a) indicates the presence of oxygenated-surface functional groups corresponding to cellulose, hemicellulose, and lignin.

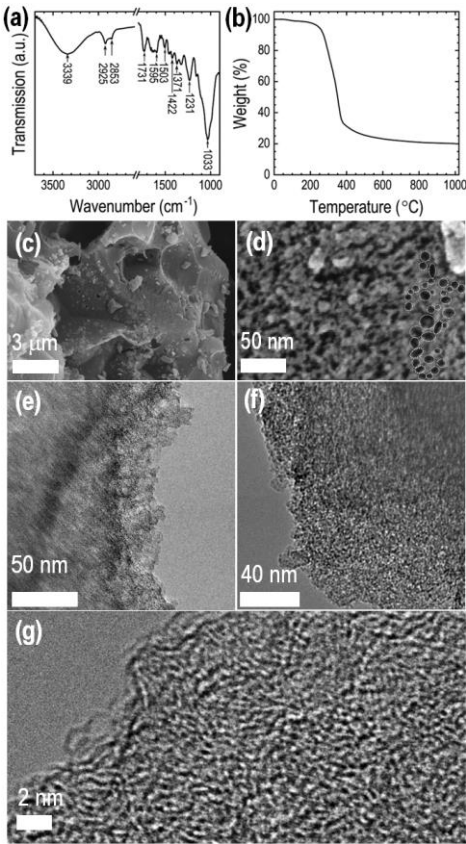


Figure 1. (a) FTIR spectrum, and (b) TGA curve of precursor, (c and d) SEM images of optimal sample, BrC_Z3_700, (e and f) TEM images of BrC_Z3_700 and (g) corresponding HR-TEM image. The dotted circles on panel d highlight the mesopores.

The broad FTIR peak centered at 3339 cm^{-1} corresponds to $-\text{OH}$ stretching vibration of

hydroxyl group from moisture content and/or alcoholic groups of cellulose and hemicellulose or phenolic groups of lignin. In addition, bands located at 2925, and 2853 cm^{-1} are due to aliphatic C–H stretching vibrations of alkyl groups in cellulose. The band at 1731 cm^{-1} corresponds to the C=O stretching vibration of acetyl groups in ester and/ or cellulose, hemicellulose and lignin.⁴¹ A weak band at 1595 and 1503 cm^{-1} correspond to aromatic C=C stretching vibration of lignin.²⁰ A band at 1422 cm^{-1} corresponds to the –OH bending of alcoholic group. Similarly, a weak band at 1371 cm^{-1} relates to the C–H bending vibration in lignin. The bands at 1231 and 1033 cm^{-1} correspond to the C–O stretching vibration of cellulose and hemi-cellulose.⁴²

The TGA curve of Barro powder (Figure 1b) has three major stages. In the initial stage (25–200 °C), weight loss occurs due to the evaporation of moisture trapped in the biomass precursor. Significant weight loss is observed in the second stage (200–380 °C) due to the pyrolytic decomposition of cellulose and hemi-cellulose components along with partial breakdown of lignin content. No observable weight loss was observed in the final stage above 380 °C. Thus, TGA result shows that Barro seed precursor can be carbonized above this temperature. In our previous work, we have prepared Barro carbons using low energy method and studied their iodine and methylene blue (dye) adsorption properties followed by the energy storage performance. The carbonization was carried out from 400 to 700 °C. We have found that the surface textural properties and adsorption and energy storage performance increase with increase in the carbonization temperature.⁴¹ Therefore, in this work, carbonization was carried out at and above 700 °C.

SEM image (Figure 1c) of the optimal sample (BrC_Z3_700) reveals large pores and irregular-shaped carbon macro particles. High-resolution SEM image (Figure 1d) shows the well-developed mesoporous structures on the surface of carbon particles. The mesopores are randomly distributed. SEM images of the directly carbonized reference sample, BrP_700 and ZnCl_2 activated Barro

carbons are supplied in the Supporting Information (Figure S1: BrP_700, Figure S2: BrC_Z1_700, Figure S3: BrC_Z2_700, Figure S4: additional SEM images of BrC_Z3_700, Figure S5: BrC_Z1_800, and Figure S6: BrC_Z1_900). Micron sized microporous surface structures are commonly observed in all the samples despite differences in the synthetic conditions. However, in high resolution SEM images, the lack of mesopores in the directly carbonized sample (Figure S1) as compared to activated carbon samples emphasizes the importance of the activating agent (ZnCl_2) for the development of pore architectures during carbonization. TEM analyses reveal the presence of some mesopores around the edge of the carbon particle (Figure 1e) and plenty of micropores with amorphous structure (Figure 1f,g) commonly realized in the biomass carbons.

Nitrogen adsorption isotherms (Figure 2a,c) reveal that nitrogen adsorption in the reference sample is very low as compared to the activated samples inferring a low specific surface area due to the lack of well-developed porosity.

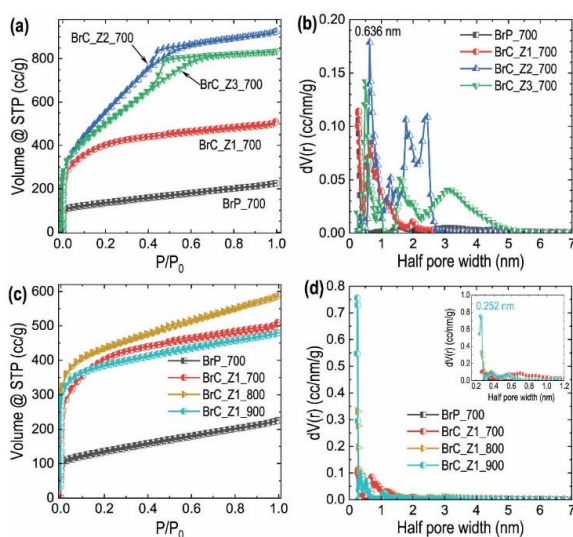


Figure 2. (a, c) Nitrogen adsorption-desorption isotherms and, (b, d) pore size distribution profiles obtained by DFT analysis of prepared carbon samples.

ZnCl_2 activated samples show much higher nitrogen uptake and the isotherms exhibit mixed type-I and type-IV behavior indicating that the hierarchical pore structure comprises of both micro

and mesopore structures. High nitrogen uptake at lower relative pressure can be attributed to the filling of micropores with the hysteresis loop at high relative pressure attributed to capillary condensation in the mesopores. Note that overall nitrogen adsorption and size of the hysteresis loop increases with increasing ZnCl_2 content suggesting the formation of more micro- and mesopores. Increasing the carbonization temperature from 700 to 800 °C significantly increases the surface area due to the formation of a large number of micropores. The micropore surface area increased significantly at 800 °C with the half pore width being as small as 0.262 nm, which can be attributed to the removal of more volatile organic matter and tar leading to the formation of abundant micropores. The smaller Zn^{2+} radius (74 pm) further contribute to obtain micropores, leading to significant increase in surface area from 700 to 800 °C. Further increase in the carbonization temperature to 900 °C reduces the specific surface due to micropore coalescence. The pore size distribution profile obtained from DFT (Figure 2b,d) shows main peaks at 0.636 and 0.295 nm, confirming microporosity. Mesoporous structure of the carbon samples was confirmed by considering BJH model where prominent peaks at 3.704 nm and 3.896 nm appear (Figure S7a,b). The textural properties of prepared carbon samples are shown in Table 1 and highlight the importance of the activating agent and the carbonization temperature in the development of hierarchical pore structures.

Table 1. Surface textural properties of Barro seed-derived nanoporous carbon materials with effects of impregnation ratio and carbonization temperature

System	SSA	S_{mic}	S_{mes}	V_{P}	V_{mic}	V_{mes}	W_{H}	D_{P}
	(m^2/g)	(m^2/g)	(m^2/g)	(cc/g)	(cc/g)	(cc/g)	(nm)	(nm)
BrP_700	719.8	616.9	102.9	0.479	0.321	0.158	0.283	3.27
BrC_Z1_700	1299.0	1184.1	114.9	0.877	0.707	0.170	0.286	3.89
BrC_Z2_700	2227.8	1568.6	659.2	2.007	1.368	0.639	0.636	3.48

BrC_Z3_700	2301.6	1580.8	720.8	1.887	1.218	0.669	0.503	3.70
BrC_Z1_800	2040.6	1855.5	185.1	1.1	0.838	0.262	0.262	3.66
BrC_Z1_900	1768.2	1652.7	115.6	0.846	0.681	0.165	0.252	3.66

SSA = total specific surface area, S_{mic} = surface area of the micropores, S_{mes} = surface area of the mesopores, V_P = total pore volume, V_{mic} = micropore volume, V_{mes} = mesopore volume, W_H = half pore width obtained from the DFT method, D_P = pore diameter estimated from BJH analysis.

Powder XRD patterns (Figure 3a) of reference and activated samples show two broad diffraction peaks at diffraction angles from 23.3-23.9 and 43.5-43.9° respectively corresponding to (002) and (100) planes of graphitized carbon materials, which is also characteristic of amorphous carbon materials prepared from biomass precursor.⁴¹ Minor diffraction peaks in the XRD pattern of the directly carbonized sample correspond to the mineral impurities present in the biomass precursor. All other samples were washed with dilute HCl and then with distilled water thoroughly to remove any residual impurities from the ZnCl₂, however, the directly carbonized sample BrP_700 was not cleaned/ washed after carbonization. Hence, some mineral impurities from precursor might have been left on carbonized sample leading to the diffraction peak at 29.3°. There are no variations in peak intensity or position of the 002 and 100 planes even though the carbonization temperature and mixing ratio were different. The change in synthetic conditions results in the formation of porous structures without any influence on the crystallinity of the materials.

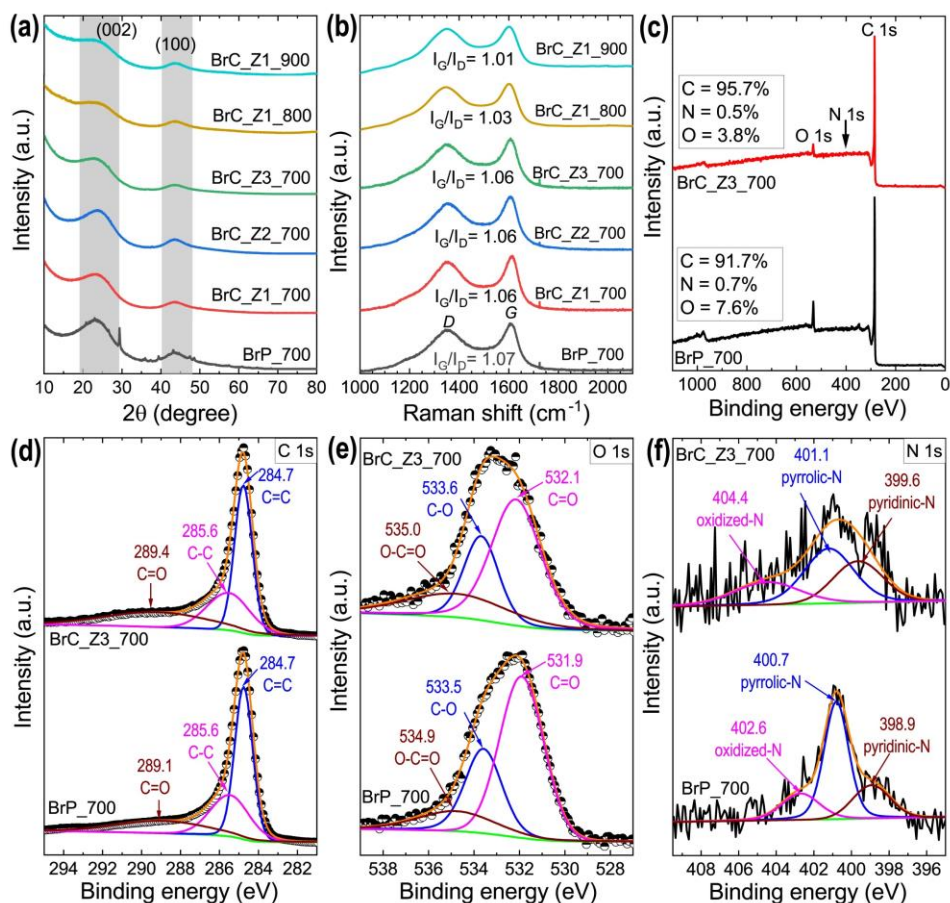


Figure 3. (a) Powder XRD patterns, (b) Raman scattering spectra, (c) XPS survey spectra, (d-f) High resolution XPS spectra of C 1s and, O 1s and N 1s of BrP_700 and BrC_Z3_700, respectively.

Raman scattering spectra (Figure 3b) of the carbon samples contain two prominent peaks positioned around 1344 and 1605 cm^{-1} . The peak at $\sim 1344 \text{ cm}^{-1}$ corresponding to D-band indicates the presence of defects in the carbon skeleton and describes the degree of amorphousness of carbon structures.⁴³ In carbon materials, the D-band corresponds to the A_{1g} symmetry and is associated with plane deformity, e.g., defects and heteroatoms. The peak at $\sim 1605 \text{ cm}^{-1}$ representing graphitic carbon (G-band) corresponds to stretching vibrations with E_{2g} symmetry of sp^2 hybridized carbon.⁴⁴ The intensity ratio between G and D bands (I_G/I_D) provides insights into structural order, and the presence of defects did not significantly change inferring that prevalence of structural defects and degree of graphitization are similar for all the samples. With an increase in

carbonization temperature, I_G/I_D ratio decreases indicating the introduction of more defects within the carbon matrix.

Surface composition was estimated by XPS analysis. XPS survey spectra (Figure 3c) of reference sample and optimal sample BrC_Z3_700 indicate that carbon, oxygen and nitrogen are the main surface elements. The deconvoluted C 1s XPS spectra (Figure 3d) contains three distinct peaks assigned to C=C (284.7 eV), C-C (285.6 eV) and C=O (289.1 eV) bonding states of carbon. The deconvoluted peak of O 1s (Figure 3e) indicates the presence of C=O (531.9 eV), C-O (533.6 eV) and O-C=O (534.9 eV) bonding. Furthermore, the deconvoluted peak of N 1s (Figure 3f) represents pyridinic N (398.9 eV), pyrrolic N (400.7 eV) and oxidized N (402.6 eV).^{29,45,46} XPS spectra show that $ZnCl_2$ causes elimination of nitrogen and oxygen from the precursor with a consequent increase in carbon content. The reason for this phenomenon is the removal of nitrogen in the form of volatile gases and hydrogen and oxygen in the form of H_2O rather than developing into hydrocarbons or oxygenated organic matters, leading to the formation of abundant pore structures.³⁵ This subsequently caused the removal of nitrogen and oxygen by yielding much higher carbon content with increased surface area in sample BrC_Z3_700 as indicated in Table 1.

Figure 4a compares the CV profiles of all the samples recorded at a scan rate of $50 \text{ mV} \cdot \text{s}^{-1}$. The CV profiles have quasi-rectangular shape, indicating an EDLC-type charge storage mechanism.⁴⁶ Weak redox peak in the CV profiles of activated samples at 0.3 and 0.4 V are attributed to the presence of oxygenated surface functional groups that lead to pseudo-capacitance. The large integrated area of the activated samples compared to the reference sample in the CV profiles indicates the high charge storage capacity of activated samples, which can be attributed to their large surface areas. Capacitance of the samples increases with increasing $ZnCl_2$ content reaching a maximum for BrC_Z3_700, which is also consistent with the porosity properties. The

CV curve emphasizes that current collection depends on the surface area of the material.

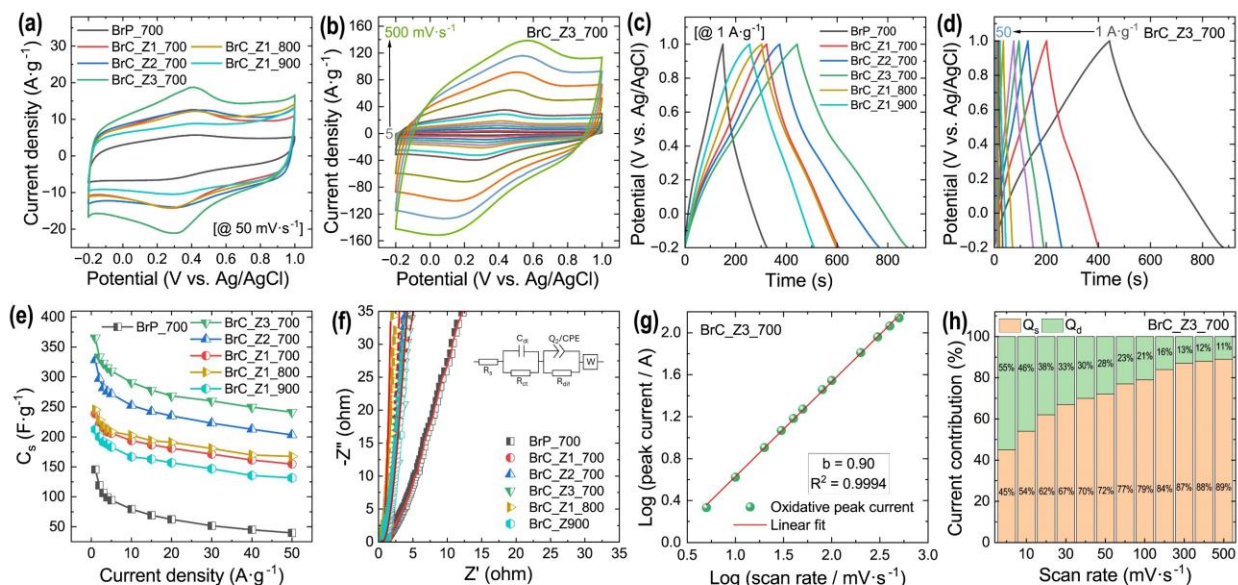


Figure 4. Electrochemical data of the prepared carbon materials. (a) CV profile at $50 \text{ mV} \cdot \text{s}^{-1}$, (b) CV profiles of the optimal sample at different scan rates, (c) GCD profiles at $1 \text{ A} \cdot \text{g}^{-1}$, (d) GCD profiles of optimal sample at different current density, (e) specific capacitance (C_s) vs. current density, (f) Nyquist plot, (g) logarithm of oxidative peak current vs. scan rate of optimal sample, and (h) surface-controlled (Q_s) and diffusion-controlled (Q_d) current contribution of BrC_Z3_700 electrode at different scan rates.

The CV profile (Figure 4b) of the optimal sample at different scan rates shows that overall current collection increases as the scan rate increases. At higher scan rates, ions in the electrolyte move more rapidly towards and away from the electrode surfaces. This rapid movement enhances the formation and dissolution of the electrical double-layer, leading to higher current. Even at higher scan rates, the quasi-rectangular shape of the CV curve is retained indicating fast ion diffusion to the electrode-electrolyte surface promoted by the hierarchical pore structures.^{46,47} CV profiles of the other materials BrP_700, BrC_Z1_700, BrC_Z2_700, BrC_Z1_800 and BrC_Z1_900 are provided in the Supporting Information (Figures S8a-e).

GCD profiles of prepared carbon samples at $1 \text{ A} \cdot \text{g}^{-1}$ current density exhibit quasi-triangular shapes indicating EDLC behavior (Figure 4c). These data indicate that BrC_Z3_700 has the

longest discharge time inferring a large energy storage capacity of the material, which is in line with its surface textural properties. The GCD curve (Figure 4d) of the optimal sample at different current densities shows shorter discharge time at higher current densities. The rate at which ions can move to and from the electrode surfaces can become a limiting factor at high current density. This dynamic effect causes a reduction in the amount of charge that can be stored and released efficiently at higher current densities, leading to a shorter discharge time. The quasi-triangular shape of GCD curve is sustained even at higher current density of $50 \text{ A} \cdot \text{g}^{-1}$, which can be attributed to pore structures that provide easy access to the electrolyte ions and promote ion diffusion at the electrode surface.^{46,47} The GCD profiles of the other materials are provided in Figures S9 (a-e). Specific capacitance (C_s) was calculated from GCD curves using eq. 1 (Figure 4e). The BrC_Z3_700 electrode achieved the maximum specific capacitance of $365.4 \text{ F} \cdot \text{g}^{-1}$ at a current density of $1 \text{ A} \cdot \text{g}^{-1}$ and retained 66.1% capacitance even at a high current density of $50 \text{ A} \cdot \text{g}^{-1}$ demonstrating the high-rate capability of this electrode material. The specific capacitance of Barro seed derived carbon is better than/comparable to other biomass derived carbons reported previously (see Table S1). A Nyquist plot (Figure 4f) obtained from EIS measurements provides information regarding the charge storage mechanism of these carbon materials. In the low frequency region, all samples gave an almost vertical line indicating EDLC behavior.⁴⁸ The EIS curves show a weak semi-circle at high frequency indicating their low charge transfer resistance. The low equivalent series resistance (ESR) values as obtained from the intersection point on the horizontal axis are $0.5 \text{ } \Omega$ (BrP_700), $0.8 \text{ } \Omega$ (BrC_Z1_700), $0.5 \text{ } \Omega$ (BrC_Z2_700), $0.4 \text{ } \Omega$ (BrC_Z3_700), and $0.3 \text{ } \Omega$ (BrC_Z1_800 and BrC_Z1_900), which indicate generally good electrical conductivity of Barro-derived carbon materials.⁴⁶ The equivalent circuit model for the directly carbonized sample shows the simple Randles circuit model modified to describe electrode

processes where both kinetics and diffusion play a role. It consists of solution resistance (R_s), a double layer capacitor C_{dl} , the charge-transfer resistance (R_{ct}), and a Warburg element (W). However, the equivalent circuit model for activated samples shows the presence of one more pair of non-ideal double layer capacitors (Q_2) / constant phase element (CPE) and diffusion resistance (R_{dif}) due to the ion-transport resistance within the internal pores. Since the ESR values of all the electrode materials were similar, differences in the electrochemical performance of these materials can be attributed to their different surface textural characteristics.

The relationship between $\log(v)$ and $\log(i)$ of BrC_Z3_700 leads to the b value of 0.90 calculated using eq. 2 (Figure 4g). Therefore, both surface-controlled and diffusion-controlled processes are involved in the charge storage mechanism.⁴⁹ However, the surface-controlled charge storage mechanism dominates at higher scan rates (Figure 4h).⁵⁰ The contribution of each charge storage mechanism was evaluated by comparing surface-controlled and diffusion-controlled energy storage as shown in Figure 4h.^{51,52} Since the BrC_Z3_700 shows the best capacitive performance of the materials studied, it was further integrated as both electrodes (anode and cathode) of a symmetrical supercapacitor cell (SSC) using aqueous electrolyte (1 M H_2SO_4). The CV profile of SSC at different scan rates in the potential window of 1.2 V is a rectangular curve indicating the electrical double-layer capacitive character of SSC (Figure 5a).⁵³ The CV curve deviates slightly from the ideal rectangular shape as scan rate increases due to charge transport resistance. The GCD profile (Figure 5b) of SSC at different current densities shows almost triangular shape indicating an EDLC charge storage mechanism. The cell has low resistance as indicated by the absence of voltage (IR) drop.⁵⁰ The C_s vs. current density curve (Figure 5c) indicates that SSC has high capacitance retention (41.2%) even at the high current density of 50 $A \cdot g^{-1}$ indicating its high-rate capability. The cyclic stability of the SSC (Figure 5d), measured at

current density of $10 \text{ A} \cdot \text{g}^{-1}$ shows outstanding cycling performance with 98.2% capacitance retention and 100% coulombic efficiency even after 10,000 charge/discharge cycles. Figure 5e shows the Nyquist plot prior to and following the cycle test where there is no significant variation indicating that there is no alteration of the electrode or electrode/electrolyte interface suggesting their extended cyclic stability.

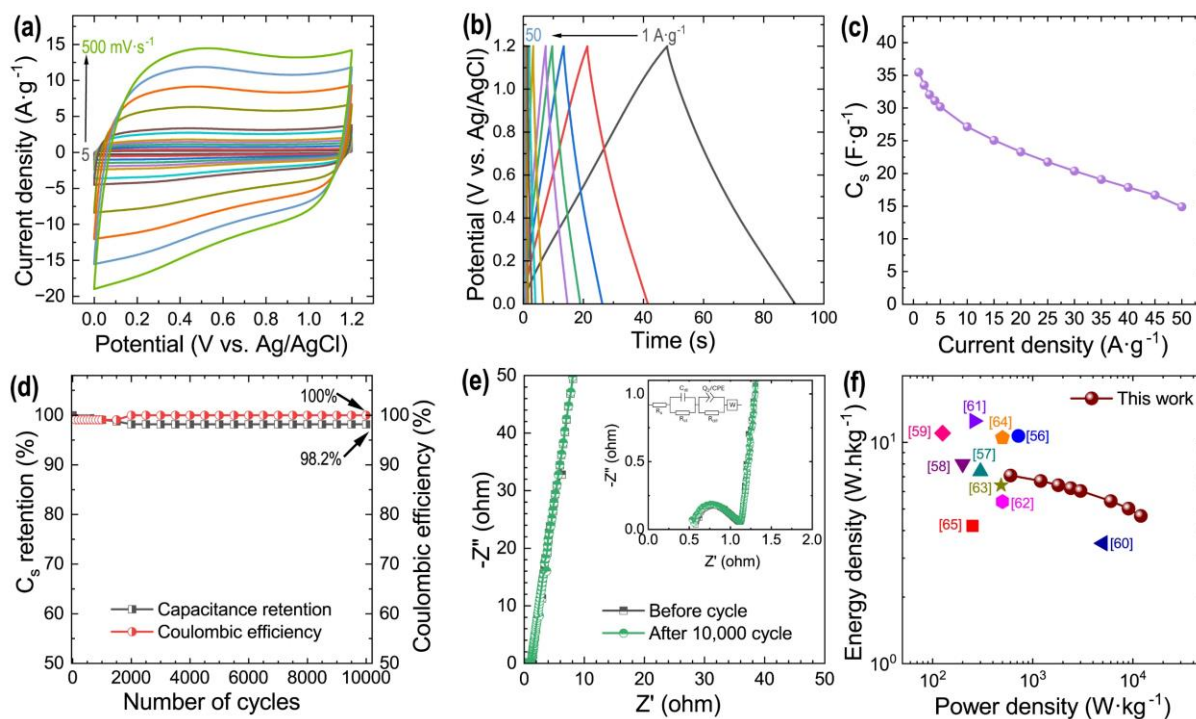


Figure 5. (a) CV curves, (b) GCD profiles, and (c) calculated specific capacitance of the cell, (d) cycle performance with Coulombic efficiency at $10 \text{ A} \cdot \text{g}^{-1}$, (e) EIS with an equivalent circuit diagram of symmetric cell, and (f) Ragone plot for comparison with previously reported biomass-derived carbons.

The semicircle observed at high frequency reflects charge transfer processes occurring at the electrode-electrolyte interface. A small semicircle indicates lower charge transfer resistance, which can be due to good conductivity of the electrode material. The linear region at low frequencies is associated with the diffusion of ions/ion transport limitation. The near-vertical line in the low frequency region represents the capacitive behavior of the electrical double-layer formed

at the electrode/electrolyte interface.^{54,55} The charge storage process is highly reversible and non-faradaic with fast ion transport that leads to negligible material degradation and consistent performance over long cycle life (10,000 charging/discharging cycles). This shows the material is highly stable with no/minimal degradation in electrode-electrolyte interface.

The power/energy density is a significantly useful measure to analyze the energy storage performance of supercapacitors and is represented in the Ragone plot (Figure 5f). BrC_Z3_700 SSC delivers a maximum energy density of $7.1 \text{ W}\cdot\text{hkg}^{-1}$ at power density of $600 \text{ W}\cdot\text{kg}^{-1}$, which is better than/comparable to previously mentioned biomass-derived carbon compounds, such as barley straw ($10.7 \text{ W}\cdot\text{hkg}^{-1}$ @ $720 \text{ W}\cdot\text{kg}^{-1}$),⁵⁶ oil palm kernel shell ($7.4 \text{ W}\cdot\text{hkg}^{-1}$ @ $300 \text{ W}\cdot\text{kg}^{-1}$),⁵⁷ tobacco waste ($8 \text{ W}\cdot\text{hkg}^{-1}$ @ $200 \text{ W}\cdot\text{kg}^{-1}$),⁵⁸ bamboo ($11 \text{ W}\cdot\text{hkg}^{-1}$ @ $126 \text{ W}\cdot\text{kg}^{-1}$),⁵⁹ chitin saccharide ($3.5 \text{ W}\cdot\text{hkg}^{-1}$ @ $5000 \text{ W}\cdot\text{kg}^{-1}$),⁶⁰ lotus seed pods ($12.5 \text{ W}\cdot\text{hkg}^{-1}$ @ $260 \text{ W}\cdot\text{kg}^{-1}$),⁶¹ bamboo-derived doped carbon ($5.4 \text{ W}\cdot\text{hkg}^{-1}$ @ $500 \text{ W}\cdot\text{kg}^{-1}$),⁶² coal tar pitch ($6.4 \text{ W}\cdot\text{hkg}^{-1}$ @ $483 \text{ W}\cdot\text{kg}^{-1}$),⁶³ chitosan ($10.5 \text{ W}\cdot\text{hkg}^{-1}$ @ $500 \text{ W}\cdot\text{kg}^{-1}$),⁶⁴ Sichuan pepper ($4.2 \text{ W}\cdot\text{hkg}^{-1}$ @ $250 \text{ W}\cdot\text{kg}^{-1}$),⁶⁵ and so on. Note that although the SSCs prepared from bamboo⁵⁹ and lotus seed pods⁶¹ showed higher energy density compared to our SSC, the power density of those cells is much lower than that of our SSC. These results demonstrate that Barro seed-derived carbon can be a promising electrode material in supercapacitor applications.

4. CONCLUSIONS

In conclusion, ZnCl_2 activated *Terminalia bellirica* seed carbonized at various temperatures and impregnation ratios yield hierarchically porous carbons with high surface area and well-defined porous architectures. The effects of mixing ratio of activating agent with the precursor plays an important role in the pore-size distribution/formation. The porous carbon fabricated at 700°C at impregnation ratio 1:3 has an ultrahigh surface area of $2301 \text{ m}^2\cdot\text{g}^{-1}$ with large pore volume of

1.887 $\text{cm}^3 \cdot \text{g}^{-1}$. The electrochemical performance of this electrode material indicates excellent capacitive performance and a large specific capacitance of $365.4 \text{ F} \cdot \text{g}^{-1}$ at current density of $1 \text{ A} \cdot \text{g}^{-1}$ in a three-electrode system. A symmetric supercapacitor cell assembled using this material could be operated in a potential window of 1.2 V in an aqueous electrolyte (1M H_2SO_4). The cell achieved specific capacitance of $35.4 \text{ F} \cdot \text{g}^{-1}$ at $1 \text{ A} \cdot \text{g}^{-1}$, with energy density of $7.1 \text{ W} \cdot \text{hkg}^{-1}$ at a power density of $600 \text{ W} \cdot \text{kg}^{-1}$ with excellent cyclic life of 98.2% after 10,000 charge/discharge cycles, demonstrating the potential of *Terminalia bellirica* seed as a sustainable carbon source to produce ultrahigh surface area nanoporous activated carbon, which can be explored for high performance supercapacitor applications.

■ ASSOCIATED INFORMATION

Supporting Information

The supporting information is available free of charge.

Additional SEM images; pore size distribution profile, additional electrochemical measurement data; table for comparative electrochemical supercapacitive performance (PDF)

■ AUTHOR INFORMATION

Corresponding Author

Lok Kumar Shrestha - *Research Center for Materials Nanoarchitectonics (MANA), National Institute for Materials Science (NIMS), 1-1 Namiki, Tsukuba, Ibaraki 305-0044, Japan; Department of Materials Science, Institute of Pure and Applied Sciences, University of Tsukuba, 1-1-1 Tennodai, Tsukuba, Ibaraki 305-8573, Japan; <https://orcid.org/0000-0003-2680-6291>;*
Email: SHRESTHA.Lokkumar@nims.go.jp

Authors

Sarita Manandhar - *Research Center for Materials Nanoarchitectonics (MANA), National Institute for Materials Science (NIMS), 1-1 Namiki, Tsukuba, Ibaraki 305-0044, Japan; Department of Materials Science, Institute of Pure and Applied Sciences, University of Tsukuba, 1-1-1 Tennodai, Tsukuba, Ibaraki 305-8573, Japan; <https://orcid.org/0009-0001-4177-9693>*

Chhabi Lal Gnawali - *Department of Applied Sciences and Chemical Engineering, Pulchowk Campus, Institute of Engineering (IOE), Tribhuvan University, 44700 Lalitpur, Nepal; <https://orcid.org/0000-0002-6554-1612>*

Rinita Rajbhandari - *Department of Applied Sciences and Chemical Engineering, Pulchowk Campus, Institute of Engineering (IOE), Tribhuvan University, 44700 Lalitpur, Nepal*

Renzhi Ma - *Research Center for Materials Nanoarchitectonics (MANA), National Institute for Materials Science (NIMS), 1-1 Namiki, Tsukuba, Ibaraki 305-0044, Japan <https://orcid.org/0000-0001-7126-2006>*

Jonathan P. Hill - *Research Center for Materials Nanoarchitectonics (MANA), National Institute for Materials Science (NIMS), 1-1 Namiki, Tsukuba, Ibaraki 305-0044, Japan; <https://orcid.org/0000-0002-4229-5842>*

Katsuhiko Ariga - *Research Center for Materials Nanoarchitectonics (MANA), National Institute for Materials Science (NIMS), 1-1 Namiki, Tsukuba, Ibaraki 305-0044, Japan; Department of Advanced Materials Science, Graduate School of Frontier Sciences, The University of Tokyo, 5-1-5 Kashiwanoha, Kashiwa, Chiba 277-8561, Japan; <https://orcid.org/0000-0002-2445-2955>*

Author Contributions

Sarita Manandhar: Writing – original draft, Investigation, Methodology, Formal analysis, Chhabi Lal Gnawali: Formal analysis, Methodology, Rinita Rajbhandari: Data curation, Formal analysis, Renzhi Ma: Methodology, Formal analysis, Jonathan P. Hill: Writing – review & editing, Katsuhiko Ariga: Writing – review & editing, Funding acquisition. Lok Kumar Shrestha: Conceptualization, Writing – review & editing, Methodology, Data curation, and Supervision.

Notes

The authors declare that they have no known competing financial interests or personal relationships that could have appeared to influence the work reported in this paper.

▪ **ACKNOWLEDGEMENTS**

This study was partially supported by Japan Society for the Promotion of Science KAKENHI Grant Numbers, JP20H00392 and JP23H05459. Authors are thankful to Dr. Pragati A. Shinde, MANA, NIMS for the technical assistance in the XPS measurements. SM is thankful to the National Institute for Materials Science (NIMS), Tsukuba, Japan for the NIMS Junior Fellowship for the Ph.D. program.

▪ **REFERENCES**

(1) Global bioenergy statistics, World bioenergy association, Sweden.
<https://www.worldbioenergy.org/global-bioenergy-statistics/> (accessed October 2024)

(2) Saini, S.; Chand, P.; Joshi, A. Biomass Derived Carbon for Supercapacitor Applications: Review. *J. Energy Storage* **2021**, *39*, 102646. <https://doi.org/10.1016/j.est.2021.102646>

(3) Yang, H.; Ye, S.; Zhou, J.; Liang, T. Biomass-Derived Porous Carbon Materials for Supercapacitor. *Front. Chem.* **2019**, *7*, 274. <https://doi.org/10.3389/fchem.2019.00274>

(4) Kumar, N.; Ghosh, S.; Thakur, D.; Lee, C. P.; Sahoo, P. K. Recent Advancements in Zero-

to Three-Dimensional Carbon Networks with a Two-dimensional Electrode Material for High-Performance Supercapacitors. *Nanoscale Adv.* **2023**, *5* (12), 3146–3176.

<https://doi.org/10.1039/d3na00094j>

(5) Lu, H.; Zhao, X. S. Biomass-derived Carbon Electrode Materials for Supercapacitors. *Sustain. Energy Fuels* **2017**, *1* (6), 1265–1281. <https://doi.org/10.1039/C7SE00099E>

(6) Zhang, Y.; Pan, H.; Zhou, Q.; Liu, K.; Ma, W.; Fan, S. Biomass-Derived Carbon for Supercapacitors Electrodes – A Review of Recent Advances. *Inorg. Chem. Commun.* **2023**, *153*, 110768. <https://doi.org/10.1016/j.inoche.2023.110768>

(7) Shinde, P. A.; Abbas, Q.; Chodankar, N. R.; Ariga, K.; Abdelkareem, M. A.; Olabi, A. G. Strengths, Weaknesses, Opportunities, and Threats (SWOT) Analysis of Supercapacitors: A Review. *J. Energy Chem.* **2023**, *79*, 611–638. <https://doi.org/10.1016/j.jechem.2022.12.030>

(8) Jiang, G.; Senthil, R. A.; Sun, Y.; Kumar, T. R.; Pan, J. Recent Progress on Porous Carbon and its Derivatives from Plants as Advanced Electrode Materials for Supercapacitors. *J. Power Sources* **2022**, *520*, 230886. <https://doi.org/10.1016/j.jpowsour.2021.230886>

(9) Mensah-Darkwa, K.; Zequine, C.; Kahol, P. K.; Gupta, R. K. Supercapacitor Energy Storage Device using Biowastes: A Sustainable Approach to Green Energy. *Sustainability* **2019**, *11* (2), 414. <https://doi.org/10.3390/su11020414>

(10) Liu, L.; Lu, C.; Ma, Y.; Yang, Y.; Li, S.; Zhu, M. Fe₂O₃@N-C@MnO₂ Composite with Chinese-Chestnut Structure for High-Performance Supercapacitors. *J. Electronic Mater.* **2023**, *52*, 4988–4999. <http://dx.doi.org/10.1007/s11664-023-10451-5>

(11) Huang, S.; Zhu, X.; Sarkar, S.; Zhao, Y. Challenges and Opportunities for Supercapacitors. *APL Mater.* **2019**, *7* (10), 100901. <https://doi.org/10.1063/1.5116146>

(12) Sengottaiyan, C.; Kalam, N. A.; Jayavel, R.; Shrestha, R. G.; Subramani, T.; Sankar, S.;

Hill, J. P.; Shrestha, L. K.; Ariga, K. BiVO₄/RGO Hybrid Nanostructure for High Performance Electrochemical Supercapacitor. *J. Solid State Chem.* **2019**, *269*, 409–418.

<https://doi.org/10.1016/j.jssc.2018.10.011>

(13) Shrestha, L. K.; Shrestha, R. G.; Hill, J. P.; Tsuruoka, T.; Ji, Q.; Nishimura, T.; Ariga, K. Surfactant-Triggered Nanoarchitectonics of Fullerene C₆₀ Crystals at a Liquid-Liquid Interface. *Langmuir* **2016**, *32* (47), 12511–12519. <https://doi.org/10.1021/acs.langmuir.6b01378>

(14) Shrestha, L. K.; Adhikari, L.; Shrestha, R. G.; Adhikari, M. P.; Adhikari, R.; Hill, J. P.; Pradhananga, R. R.; Ariga, K. Nanoporous Carbon Materials with Enhanced Supercapacitance Performance and Non-Aromatic Chemical Sensing with C₁/C₂ Alcohol Discrimination. *Sci. Technol. Adv. Mater.* **2016**, *17* (1), 483–492. <https://doi.org/10.1080/14686996.2016.1219971>

(15) Zhu, M.; Tu, C.; Li, X.; Luo, Q.; Li, S. In Situ Formation of MnO@N-doped Carbon for Asymmetric Supercapacitor with Enhanced Cycling Performance. *Mater. Chem. Front.* **2022**, *6*, 491-502. <https://doi.org/10.1039/D1QM01404H>

(16) Chen, T. W.; Chen, S. M.; Anushya, G.; Kannan, R.; Veerakumar, P.; Al-Sehemi, A. G.; Mariyappan, V.; Alargarsamy, S.; Alam, M. M.; Mahesh, T. C.; Ramachandran, R.; Kalimuthu, P. Electrochemical Energy Storage Applications of Functionalized Carbon-based Nanomaterials: An Overview. *Int. J. Electrochem. Sci.* **2024**, *19* (5), 100548.

<https://doi.org/10.1016/j.ijoes.2024.100548>

(17) Shrestha, R. G.; Shrestha, L. K.; Ariga, K. Carbon Nanoarchitectonics for Energy and Related Applications. *C-J. Carbon Res.* **2021**, *7* (4), 73. <https://doi.org/10.3390/c7040073>

(18) Khalafallah, D.; Zhang, Q. Dual-metal hydroxide Heterojunction and Chayote Fruit Biomass-derived Hierarchical Porous Carbon for Augmenting the Performance of Hybrid Supercapacitors. *J. Energy Storage.* **2024**, *91*, 112621. <https://doi.org/10.1016/j.est.2024.112621>

(19) Khalafallah, D.; Ibrahim, N.; Mohammed, L.; Zhang, Q. Z-scheme Heterostructures Confining rGO/protonated C_3N_5 junction Supported CoCu LDH Positive Electrode and Fe_3O_4 Negative Electrode for Supercapacitors. *Carbon* **2025**, *231*, 119683. <https://doi.org/10.1016/j.carbon.2024.119683>

(20) Wang, T.; Hu, S.; Wu, D.; Zhao, W.; Yu, W.; Wang, M.; Xu, J.; Zhang, J. Boosting the Capacity of Biomass-based Supercapacitors using Carbon Materials of Wood Derivatives and Redox Molecules from Plants. *J. Mater. Chem. A* **2021**, *9* (19), 11839–11852. <https://doi.org/10.1039/D1TA01542G>

(21) Wang, J.; Zhang, Q.; Deng, M. Eco-Friendly Preparation of Biomass-Derived Porous Carbon and its Electrochemical Properties. *ACS Omega* **2022**, *7* (26), 22689–22697. <https://doi.org/10.1021/acsomega.2c02140>

(22) Shrestha, R. G.; Maji, S.; Shrestha, L. K.; Ariga, K. Nanoarchitectonics of Nanoporous Carbon Materials in Supercapacitors Applications. *Nanomaterials* **2020**, *10* (4), 639. <https://doi.org/10.3390/nano10040639>

(23) Gnawali, C. L.; Shrestha, L. K.; Hill, J. P.; Ma, R.; Ariga, K.; Adhikari, M. P.; Rajbhandari, R.; Pokharel, B. P. Nanoporous Activated Carbon Material from *Terminalia chebula* Seed for Supercapacitor Application. *C-J. Carbon Res.* **2023**, *9* (4), 109. <https://doi.org/10.3390/c9040109>

(24) Shrestha, R. G.; Maji, S.; Mallick, A. K.; Jha, A.; Shrestha, R. M.; Rajbhandari, R.; Hill, J. P.; Ariga, K.; Shrestha, L. K. Hierarchically Porous Carbon from *Phoenix dactylifera* Seed for High-Performance Supercapacitor Applications. *Bull. Chem. Soc. Jpn.* **2022**, *95* (7), 1060–1067. <https://doi.org/10.1246/bcsj.20220129>

(25) Arkhipova, E. A.; Novotortsev, R. Y.; Ivanov, A. S.; Maslakov, K. I.; Savilov, S. V. Rice Husk-Derived Activated Carbon Electrode in Redox-Active Electrolyte – New Approach for

Enhancing Supercapacitor Performance. *J. Energy Storage* **2022**, *55*, 105699.
<https://doi.org/10.1016/J.EST.2022.105699>

(26) Song, M.; Zhou, Y.; Ren, X.; Wan, J.; Du, Y.; Wu, G.; Ma, F. Biowaste-based Porous Carbon for Supercapacitor: The Influence of Preparation Processes on Structure and Performance. *J. Colloid. Interface Sci.* **2019**, *535*, 276–286. <https://doi.org/10.1016/j.jcis.2018.09.055>

(27) Wang, B.; Wu, X.; Yu, Y.; Wang, N.; Zhou, Z. Simultaneously Tuning the Hierarchical Porous Structure and Graphitization Degree of Biomass Derived Carbon for Supercapacitors. *Electrochim. Acta* **2022**, *432*, 141219. <https://doi.org/10.1016/j.electacta.2022.141219>

(28) Devi, R.; Kumar, V.; Kumar, S.; Sisodiya, A. K.; Mishra, A. K.; Jatana, A.; Kumar, A.; Singh, P. Development of Activated Carbon by Bio Waste Material for Application in Supercapacitor Electrodes. *Mater. Lett.* **2023**, *335*, 133830.
<https://doi.org/10.1016/j.matlet.2023.133830>

(29) Dhakal, G.; Kumar, D. R.; Sahoo, S.; Shim, J. J. Litchi Seed Biowaste-Derived Activated Carbon Supporting Matrix for Efficient Symmetric and Asymmetric Supercapacitors. *Carbon* **2023**, *208*, 277–289. <https://doi.org/10.1016/j.carbon.2023.03.045>

(30) Yuksel, R.; Karakehya, N. High Energy Density Biomass-Derived Activated Carbon Materials for Sustainable Energy Storage. *Carbon* **2024**, *221*, 118934.
<https://doi.org/10.1016/j.carbon.2024.118934>

(31) Zhu, M.; Yang, Y.; Ma, Y. Salt-Assisted Synthesis of Advanced Carbon-Based Materials for Energy-related Applications. *Green Chem.* **2023**, *25*, 10263-10303.
<https://doi.org/10.1039/D3GC03080F>

(32) Khalafallah, D.; Quan, X.; Ouyang, C.; Zhi, M.; Hong, Z. Heteroatoms Doped Porous Carbon Derived from Waste Potato Peel for Supercapacitors. *Renew. Energy*. **2021**, *170*, 60–71.

<https://doi.org/10.1016/j.renene.2021.01.077>

(33) Khalafallah, D.; Zhang, Y.; Dai, H.; Liu, C.; Qinfang, Z. Manipulating the overall capacitance of hierarchical porous carbons via structure- and pore-tailoring approach. *Carbon* **2024**, 227, 119250. <https://doi.org/10.1016/j.carbon.2024.119250>

(34) Bosch, D.; Back, J. O.; Gurtner, D.; Giberti, S.; Hofmann, A.; Bockreis, A. Alternative Feedstock for the Production of Activated Carbon with ZnCl₂: Forestry Residue Biomass and Waste Wood. *Carbon Resour. Convers.* **2022**, 5 (4), 299–309. <https://doi.org/10.1016/j.crcon.2022.09.001>

(35) Han, G.; Jia, J.; Liu, Q.; Huang, G.; Xing, B.; Zhang, C.; Cao, Y. Template-Activated Bifunctional Soluble Salt ZnCl₂ Assisted Synthesis of Coal-Based Hierarchical Porous Carbon for High-Performance Supercapacitors. *Carbon* **2022**, 186, 380–390. <https://doi.org/10.1016/j.carbon.2021.10.042>

(36) Fan, M.; Shao, Y.; Wang, Y.; Sun, J.; He, H.; Jiang, Y.; Zhang, S.; Wang, Y.; Hu, X. Preparation of Activated Carbon with Recycled ZnCl₂ for Maximizing Utilization Efficiency of the Activating Agent and Minimizing Generation of Liquid Waste. *Chem. Eng. J.* **2024**, 500, 157278. <https://doi.org/10.1016/j.cej.2024.157278>

(37) Wu, S.; Wei, D.; Cui, H.; Wang, H.; Li, Y.; Tao, X.; Yan, C.; Liu, C. Electrochemical Performance of Polyacrylamide Hydrogel Based Nitrogen-Doped Porous Carbon for Supercapacitor. *J. Electroanal. Chem.* **2020**, 865, 114141. <https://doi.org/10.1016/J.JELECHEM.2020.114141>

(38) Kshetri, T.; Tran, D. T.; Singh, T. I.; Kim, N. H.; Lau, K.; Lee, J. H. Effects of The Composition of Reduced Graphene Oxide/Carbon Nanofiber Nanocomposite on Charge Storage Behaviors. *Compos. B Eng.* **2019**, 178, 107500.

<https://doi.org/10.1016/j.compositesb.2019.107500>

(39) Chen, T.; Wang, F.; Cao, S.; Bai, Y.; Zheng, S.; Li, W.; Zhang, S.; Hu, S. X.; Pang, H. In Situ Synthesis of MOF-74 Family for High Areal Energy Density of Aqueous Nickel–Zinc Batteries. *Adv. Mater.* **2022**, *34* (30), 2201779. <https://doi.org/10.1002/adma.202201779>

(40) Liu, C.; Bai, Y.; Li, W.; Yang, F.; Zhang, G.; Pang, H. In Situ Growth of Three-Dimensional Mxene/Metal–Organic Framework Composites for High-Performance Supercapacitors. *Angew. Chem. Int. Ed.* **2022**, *61* (11), E202116282. <https://doi.org/10.1002/anie.202116282>

(41) Gnawali, C. L.; Manandhar, S.; Shahi, S.; Shrestha, R. G.; Adhikari, M. P.; Rajbhandari, R.; Pokharel, B. P.; Ma, R.; Ariga, K.; Shrestha, L. K. Nanoporous Carbon Materials from *Terminalia bellirica* Seed for Iodine and Methylene Blue Adsorption and High-Performance Supercapacitor Applications. *Bull. Chem. Soc. Jpn.* **2023**, *96* (6), 572–581. <https://doi.org/10.1246/bcsj.20230093>

(42) Salim, R. Md.; Asik, J.; Sarjadi, M. S. Chemical Functional Groups of Extractives, Cellulose and Lignin Extracted from Native *Leucaena leucocephala* Bark. *Wood Sci. Technol.* **2021**, *55* (2), 295–313. <https://doi.org/10.1007/s00226-020-01258-2>

(43) Thangavel, R.; Kaliyappan, K.; Ramasamy, H. V.; Sun, X.; Lee, Y. S. Engineering the Pores of Biomass-Derived Carbon: Insights for Achieving Ultrahigh Stability at High Power in High-Energy Supercapacitors. *ChemSusChem* **2017**, *10* (13), 2805–2815. <https://doi.org/10.1002/cssc.201700492>

(44) Kosateva, A.; Stoycheva, I.; Petrova, B.; Tsyntsarski, B. Characterization of some Carbon Materials by Raman Spectroscopy. *Bulg. Chem. Commun.* **2021**, *53* (A), 85–88. <https://doi.org/10.34049/bcc.53.A.0011>

(45) Zhu, M.; Lan, J.; Zhang, X.; Sui, G.; Yang, X. Porous Carbon Derived From: *Ailanthus*

altissima with Unique Honeycomb-like Microstructure for High-Performance Supercapacitors. *New J. Chem.* **2017**, *41* (11), 4281–4285. <https://doi.org/10.1039/c7nj01127j>

(46) Liu, H.; Zhang, F.; Lin, X.; Wu, J.; Huang, J. A Hierarchical Integrated 3D Carbon Electrode Derived from Ginkgo Leaves via Hydrothermal Carbonization of H₃PO₄ for High-Performance Supercapacitors. *Nanoscale Adv.* **2023**, *5* (3), 786–795. <https://doi.org/10.1039/d2na00758d>

(47) Rajesh, M.; Manikandan, R.; Park, S.; Kim, B. C.; Cho, W. J.; Yu, K. H.; Raj, C. J. Pinecone Biomass-Derived Activated Carbon: The Potential Electrode Material for the Development of Symmetric and Asymmetric Supercapacitors. *Int. J. Energy Res.* **2020**, *44* (11), 8591–8605. <https://doi.org/10.1002/er.5548>

(48) Shao, Y.; El-Kady, M. F.; Sun, J.; Li, Y.; Zhang, Q.; Zhu, M.; Wang, H.; Dunn, B.; Kaner, R. B. Design and Mechanisms of Asymmetric Supercapacitors. *Chem. Rev.* **2018**, *118* (18), 9233–9280. <https://doi.org/10.1021/acs.chemrev.8b00252>

(49) Yang, Y.; Chen, D.; Han, W.; Cheng, Y.; Sun, B.; Hou, C.; Zhao, G.; Liu, D.; Chen, G.; Han, J.; Zhang, X. Nature-Inspired Self-Activation Method for the Controllable Synthesis of Highly Porous Carbons for High-performance Supercapacitors. *Carbon* **2023**, *205*, 1–9. <https://doi.org/10.1016/j.carbon.2023.01.013>

(50) Wang, S.; Li, L.; Wang, H.; Wang, X.; Wang, T. Continuous and Scalable Manufacture of Coal-Derived Hierarchical Porous Carbon Dominated with Mesopores for High Rate-Performance Supercapacitors. *ACS Appl. Energy Mater.* **2024**, *7* (9), 4268–4278. <https://doi.org/10.1021/acsaem.4c00711>

(51) Manikandan, R.; Raj, C. J.; Nagaraju, G.; Velayutham, R.; Moulton, S. E.; Puigdollers, J.; Kim, B. C. Selenium Enriched Hybrid Metal Chalcogenides with Enhanced Redox Kinetics for High-Energy Density Supercapacitors. *Chem. Eng. J.* **2021**, *414*, 128924.

<https://doi.org/10.1016/J.CEJ.2021.128924>

(52) Bhattarai, R. M.; Chhetri, K.; Natarajan, S.; Saud, S.; Kim, S. J.; Mok, Y. S. Activated Carbon Derived from Cherry Flower Biowaste with a Self-Doped Heteroatom and Large Specific Surface Area for Supercapacitor and Sodium-Ion Battery Applications. *Chemosphere* **2022**, *303*, 135290. <https://doi.org/10.1016/J.CHEMOSPHERE.2022.135290>

(53) Magana, J. R.; Kolen'Ko, Y. V.; Deepak, F. L.; Solans, C.; Shrestha, R. G.; Hill, J. P.; Ariga, K.; Shrestha, L. K.; Rodriguez-Abreu, C. From Chromonic Self-Assembly to Hollow Carbon Nanofibers: Efficient Materials in Supercapacitor and Vapor-Sensing Applications. *ACS Appl. Mater. Interfaces* **2016**, *8* (45), 31231–31238. <https://doi.org/10.1021/acsami.6b09819>

(54) Mei, B. A.; Munteshari, O.; Lau, J.; Dunn, B.; Pilon, L. Physical Interpretations of Nyquist Plots for EDLC Electrodes and Devices. *J. Phys. Chem. C* **2018**, *122* (1), 194–206. <https://doi.org/10.1021/acs.jpcc.7b10582>

(55) Hamouda, H. A.; Cui, S.; Dai, X.; Xiao, L.; Xie, X.; Peng, H.; Ma, G. Synthesis of Porous Carbon Material based on Biomass Derived from Hibiscus Sabdariffa fruits as Active Electrodes for High-Performance Symmetric Supercapacitors. *RSC Adv.* **2020**, *11* (1), 354–363. <https://doi.org/10.1039/d0ra09509e>

(56) Ebrahimi, M.; Hosseini-Monfared, H.; Javanbakht, M.; Mahdi, F. Biomass-Derived Nanostructured Carbon Materials for High-Performance Supercapacitor Electrodes. *Biomass Convers. Biorefin.* **2024**, *14*, 17363–17380. <https://doi.org/10.1007/s13399-022-03733-1>

(57) Misnon, I. I.; Zain, N. K. M.; Jose, R. Conversion of Oil Palm Kernel Shell Biomass to Activated Carbon for Supercapacitor Electrode Application. *Waste Biomass Valor.* **2019**, *10* (6), 1731–1740. <https://doi.org/10.1007/s12649-018-0196-y>

(58) Chen, H.; Guo, Y. C.; Wang, F.; Wang, G.; Qi, P. R.; Guo, X. H.; Dai, B.; Yu, F. An

Activated Carbon Derived from Tobacco Waste for use as a Supercapacitor Electrode Material. *New Carbon Mater.* **2017**, 32 (6), 592–599. [https://doi.org/10.1016/S1872-5805\(17\)60140-9](https://doi.org/10.1016/S1872-5805(17)60140-9)

(59) Nguyen, T. B.; Yoon, B.; Nguyen, T. D.; Oh, E.; Ma, Y.; Wang, M.; Suhr, J. A Facile Salt-Templating Synthesis Route of Bamboo-Derived Hierarchical Porous Carbon for Supercapacitor Applications. *Carbon* **2023**, 206, 383–391. <https://doi.org/10.1016/j.carbon.2023.02.060>

(60) Deshpande, A.; Rawat, S.; Patil, I. M.; Rane, S.; Bhaskar, T.; Ogale, S. B.; Hotha, S. Converting Renewable Saccharides to Heteroatom Doped Porous Carbons as Supercapacitor Electrodes. *Carbon* **2023**, 214, 118368. <https://doi.org/10.1016/j.carbon.2023.118368>

(61) Liu, B.; Zhou, X.; Chen, H.; Liu, Y.; Li, H. Promising Porous Carbons Derived from Lotus Seedpods with Outstanding Supercapacitance Performance. *Electrochim. Acta* **2016**, 208, 55–63. <https://doi.org/10.1016/j.electacta.2016.05.020>

(62) Abbas, S. C.; Lin, C.; Hua, Z.; Deng, Q.; Huang, H.; Ni, Y.; Cao, S.; Ma, X. Bamboo-Derived Carbon Material Inherently Doped with SiC and Nitrogen for Flexible Supercapacitors. *Chem. Eng. J.* **2022**, 433 (3), 133738. <https://doi.org/10.1016/J.CEJ.2021.133738>

(63) Jiang, Y.; He, Z.; Cui, X.; Liu, Z.; Wan, J.; Liu, Y.; Ma, F. Hierarchical Porous Carbon Derived from Coal Tar Pitch by One Step Carbonization and Activation Combined with a CaO Template for Supercapacitors. *New J. Chem.* **2022**, 46 (13), 6078–6090. <https://doi.org/10.1039/d2nj00433j>

(64) Chen, K.; Weng, S.; Lu, J.; Gu, J.; Chen, G.; Hu, O.; Jiang, X.; Hou, L. Facile Synthesis of Chitosan Derived Heteroatoms-Doped Hierarchical Porous Carbon for Supercapacitors. *Microporous Mesoporous Mater.* **2021**, 320, 111106. <https://doi.org/10.1016/J.MICROMESO.2021.111106>

(65) Zhang, H.; Xiao, W.; Zhou, W.; Chen, S.; Zhang, Y. Hierarchical Porous Carbon Derived

1
2
3
4
5
6
7
8
9
10
11
12
13
14
15
16
17
18
19
20
21
22
23
24
25
26
27
28
29
30
31
32
33
34
35
36
37
38
39
40
41
42
43
44
45
46
47
48
49
50
51
52
53
54
55
56
57
58
59
60

from Sichuan Pepper for High-Performance Symmetric Supercapacitor with Decent Rate
Capability and Cycling Stability. *Nanomaterials* **2019**, *9* (4), 553.
<https://doi.org/10.3390/nano9040553>